Numerical investigation of an extra-deep drawing process with industrial parameters: formability analysis and process optimization

Amina Belguebli
Laboratory of Mechanics and Energy (LME), Mechanical Engineering Department, Faculty of Technology, Hassiba Benbouali University of Chlef, Algeria
a.belguebli@univ-chlef.dz, https://orcid.org/0000-0002-0463-2094

Ibrahim Zidane, Adel Hadj Amar
Laboratory of Rheology and Mechanics (LRM), Mechanical Engineering Department, Faculty of Technology, Hassiba Benbouali University of Chlef, Algeria
i.zidane@univ-chlef.dz, https://orcid.org/0000-0002-4222-5617
a.hadj94@univ-chlef.dz, https://orcid.org/0000-0002-7594-3762

Abdessoufi Benhamou
Laboratory of Mechanics and Energy (LME), Mechanical Engineering Department, Faculty of Technology, Hassiba Benbouali University of Chlef, Algeria
a.benhamou@univ-chlef.dz, https://orcid.org/0000-0002-8547-5915

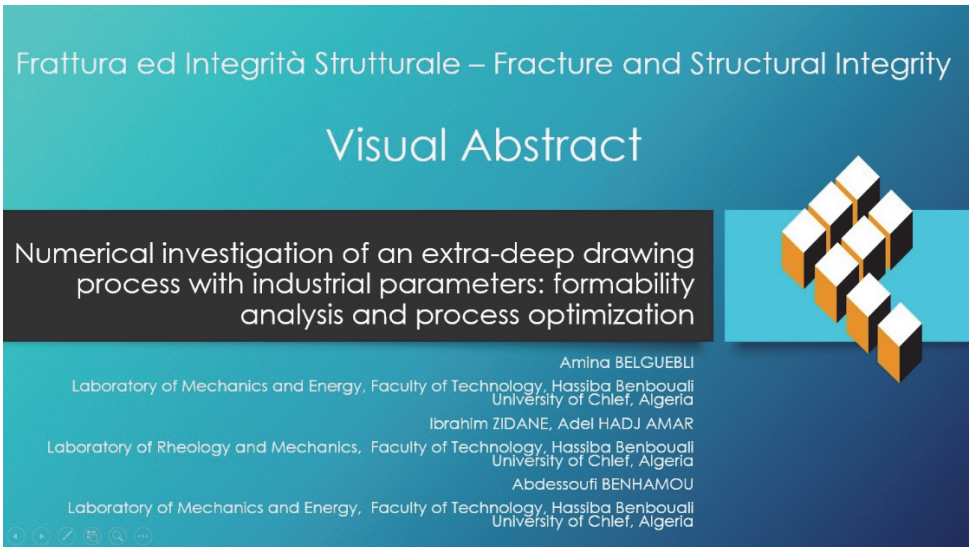

KEYWORDS. Extra-deep drawing, Experimental works, Numerical analysis, Rupture, Wrinkling, Wheelbarrow tray.

Citation: Belguebli, A., Zidane, I., Hadj Amar, A., Benhamou, A., Numerical investigation of an extra-deep drawing process with industrial parameters: formability analysis and process optimization, Frattura ed Integrità Strutturale, 68 (2024) 45-62.

Received: 18.10.2023
Accepted: 02.01.2024
Published: 17.01.2024
Issue: 04.2024

INTRODUCTION

Manufacturing through the extra-deep drawing of sheet metals is a widely adopted technology across various industrial sectors, particularly in household appliances, automobile construction, and civil engineering. This process has seen extensive development owing to its widespread application in industry. In recent years, to meet the needs of manufacturers in terms of quality and competitiveness, many investigations have been devoted to the numerical simulation of this process in order to optimize and ensure product feasibility [1–3].

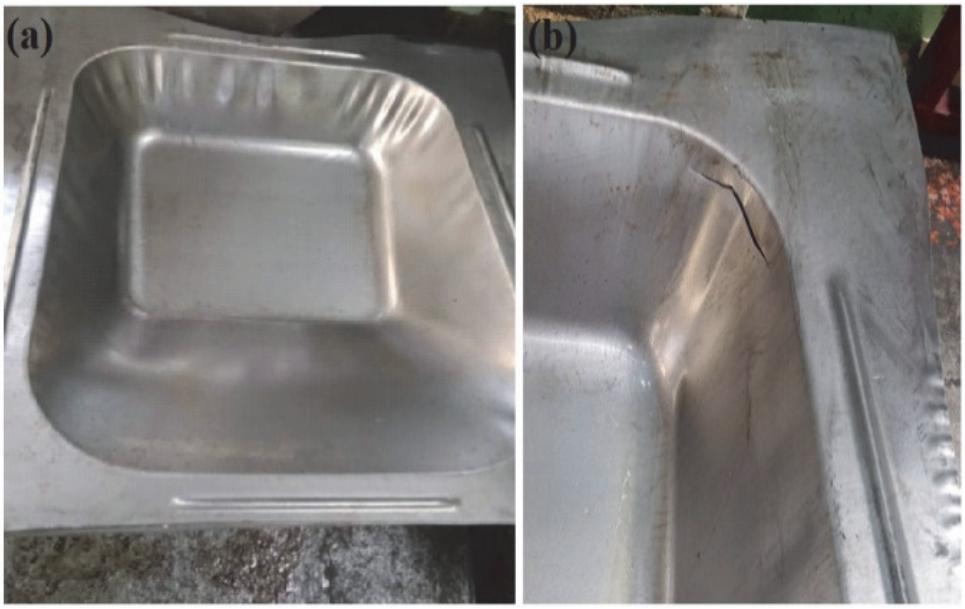

Figure 1: Appearance of rupture and wrinkling in extra-deep drawing of wheelbarrow trays.

At a local company, EIMS-Miliana-Algeria [4], extra-deep drawing is intensively used to manufacture products with relatively complex shapes. The products and components manufactured at this company are: - bathtubs and kitchen sinks of different sizes in enameled cold-rolled steels, - some gas heating and two-burner flat stove components, - light pole reflector, - ceiling lighting for office, wheelbarrow - and capos for outdoor lamps. The company's specific goal is to minimize scrap due to defects to save costs and time. These defects are wrinkling and rupture, more specifically in the forming of the wheelbarrow tray (Fig. 1). Rupture involves fracture or tearing, typically due to inadequate control of the blank holder pressure (BHP) or poorly lubricated contacts, leading to excessive frictional stress and inappropriate deep drawing rates. Wrinkling occurs as undulations on the deformed part due to compressive stresses, even in non-contact zones with deep drawing tools (punch, die, and blank holder). This phenomenon arises from various factors, including low BHP, large gaps between die and punch, existing tool defects, excessive distance between the blank holder and die, and over-lubrication. Tiwari et al. [5] discussed factors affecting deep drawing, including tool geometries, friction, blank holders, lubrication, and temperature. Additionally, Atul and Babu [6] pointed out that necking and wrinkling are influenced by the same factors. Candra et al. [7] conducted both analytical and numerical studies on the force applied to the blank holder to prevent rupture and enhance formability in deep drawing. Sorrentino et al. [8,9] explored wrinkling, necking, and rupture in thin sheet metal forming using a forming limit curve under different friction conditions. They introduced patchwork blanks as a new method to achieve a more uniform thickness in the formed part. Also studying friction conditions, Neto et al. [10] used numerical simulations to study the influence of friction as a function of pressure on wrinkling in the deep drawing process. In the numerical and experimental study conducted on cold deep drawing, Bahanan et al. [11] indicated that the friction coefficient has a significant influence on the process. They showed that rupture, in the form of tears or splits, can be avoided if the elements located near the die surface flow more easily compared to those near the punch. Kim et al. [12] evaluated lubricants in deep drawing tests, emphasizing the role of good lubrication in reducing wrinkling, rupture, and localized thinning, as well as minimizing tool wear in high-volume production. Pan et al. [13] demonstrated that lubricants containing graphene nanosheets in ethanol can reduce friction and enhance surface quality, thereby minimizing wrinkling.

Successful deep-drawn parts require the careful management of the factors mentioned above to prevent wrinkling and rupture, which are commonly encountered in the manufacturing industry [5,14]. Effective BHP control is crucial to avoid defects and manage material plastic flow during sheet metal forming [15]. Additionally, lubricants are used in the plank-die contact zone in some industrial cases, facilitating easier sheet flow into the die with the presence of the blank-holder. In order to find a semi-finished product free from defects, operators react to the BHP of a deep drawing press machine's according to their experience. This observation was noticed by ourselves in the EIMS company and was documented by Heingärtner et al. [16]. These manual interventions can significantly increase scrap generation and press line downtime, resulting in wasted time and cost. Furthermore, experimental methods do not always lead to a successful semi-finished product. Nowadays, numerical analysis based on the FE method offers a better understanding of deep drawing processes [17], enabling the prediction of forming defects [18,19] and providing insights into deformed shape, stress and strain distribution, and punch loading [20–22]. This technique is now of real economic interest for time and cost savings.
To model a deep drawing operation, in addition to the modeling the process itself (including geometries, tool actions and speeds, temperature, etc.), it is necessary to incorporate the following components into numerical simulation software [23,24]: - an elastoplastic behavior laws describing the sheet metal's mechanical response, - a friction law expressing the sheet metal-tool contacts, whether dry or lubricated, - and a forming limit curve or damage law describing the sheet metal's rupture during forming.
In this study, a numerical simulation of the extra-deep drawing process of a wheelbarrow tray was performed using ABAQUS/Explicit FE software with industrial parameters from the EIMS company. DC06EK cold-rolled steel was used with a sheet thickness of 1.6 mm. In Section 2, 3D measurements are performed on a defect-free manufactured wheelbarrow tray. The dimensions were measured using the reverse engineering process using a 3D scanner and an ultrasonic thickness gauge. This step served to produce the complex geometric shape of the punch and to validate the numerical approach. Following this, Section 3 outlines the results of tensile tests aimed at characterizing the parameters of the work hardening law and an anisotropic yield criterion. These parameters are subsequently introduced into the numerical model. Additionally, Section 4 covers the tribological test, providing essential data on the coefficient of friction to feed the numerical model. Section 5 details the numerical modeling steps of the extra-deep drawing process, namely geometry, mesh, material, tool-blank contacts, and boundary conditions. In the result section after validation, the influence of BHP on rupture and wrinkling is investigated.

EXPERIMENTAL WORKS

Measurements

In this part of the study, the CREAFORM HandySCAN300 professional 3D laser scanner was used to perform 3D measurements, as shown in Fig. 2-a. This scanner is a standalone device with several key features, including an accuracy of 0.04mm, a large scanning area with 11 laser crosses, and a high measurement rate of up to 205,000 measurements/s. In addition, it is widely used in the manufacturing and metrology industries. Using this 3D device, both the outer and inner surfaces of the wheelbarrow tray were scanned. It was found that relying solely on the assembly of the two outer and inner surfaces did not yield accurate measurements of the wheelbarrow tray's thickness. Hence, additional ultrasonic thickness measurements were carried out to complement the 3D laser scanning, as depicted in Fig. 2-b. These measurements will serve as a basis for comparison with the numerical results. The ultrasonic thickness measurements were performed using the "Sofranel EHC 09B" device, a metrological measuring instrument. This device offers instantaneous digital measurements by analyzing the return time of an ultrasonic wave emitted into the object and received by the sensor. With a measuring range spanning from 0.2 to 508mm and a resolution of 0.01mm, the Sofranel EHC 09B proved highly suitable for assessing the thickness reduction of the deep-drawn wheelbarrow tray.

Mechanical properties of the DC06EK

The extra-deep drawing steel DC06EK (DIN EN10209:1998, Material No. 1.0869) with a sheet thickness of 1.6 mm was used to perform the experiments. This sheet metal is steel with a low carbon content dedicated to enameling by vitrification. Uniaxial tensile tests were conducted on a universal testing machine, operating at a constant velocity of 1 mm/min with a capacity of 50 kN. Tensile specimens were extracted from a DC06EK steel sheet with a thickness of 1.6 mm, oriented at 0°, 45°, and 90° to the rolling direction (RD) following the ASTM E8 standard [25]. These specimens were manufactured using a water jet cutting machine (see Fig. 3), which provides greater precision by extracting them from a thin sheet measuring 1.6 mm in thickness. Using traditional machines like a milling machine for manufacturing can introduce

significant machining defects and distortions due to the thin sheet metal, potentially impacting the necking or rupture behavior during tensile tests. The useful part of the specimens was filmed with an acquisition speed of 2 images/s. The plastic strains were subsequently obtained in post-processing by the digital image correlation technique. Additionally, the force/displacement/time data were recorded directly from the tensile testing machine (Fig. 4).

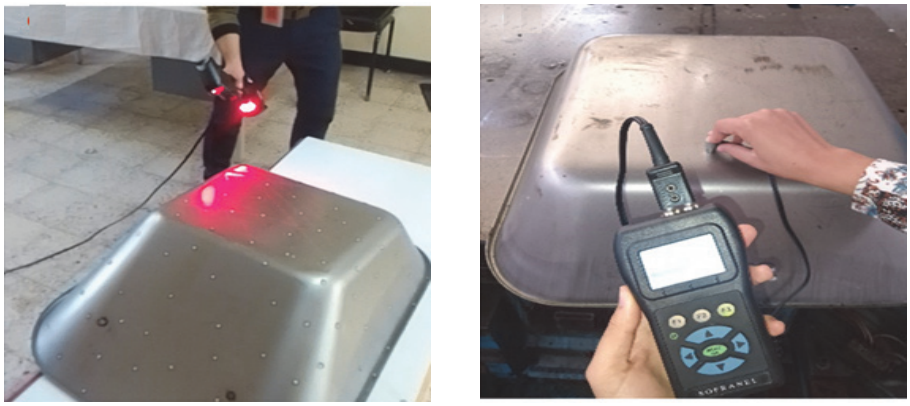

(a) (b)

Figure 2: 3D measurements: (a) CREAFORM HandySCAN300 3D laser scanner, (b) Ultrasound thickness measurements using the Sofranel EHC 09B device.

Figure 3: Cutting the specimens using the water jet process.

Lankford's r-values (average anisotropy coefficient) were employed to study anisotropy, reflecting the relationship between transverse plastic strain ε_2 and plastic strain in the thickness ε_3:

$$r = \frac{\varepsilon_2}{\varepsilon_3} = -\frac{\varepsilon_2}{\varepsilon_1 + \varepsilon_2} \tag{1}$$

Plastic strain in the thickness is calculated using the volume conservation assumption: $\varepsilon_3=-(\varepsilon_1+\varepsilon_2)$. The Lankford's r-values for each orientation were calculated as per the ISO 10113:2020 standard [26] and reported in Tab. 1. The Hill48 anisotropic yield criterion [27] was used in the "Numerical Modeling" section. The Hill48 criterion, under the hypothesis of plane stresses, can be written as follows:

$$\bar{\sigma}\left(\sigma_{ij}\right) = \sqrt{\sigma_{XX}^2(H+G) + \sigma_{YY}^2(H+F) - 2H\sigma_{XX}\sigma_{YY} + 2N\sigma_{XY}^2} \tag{2}$$

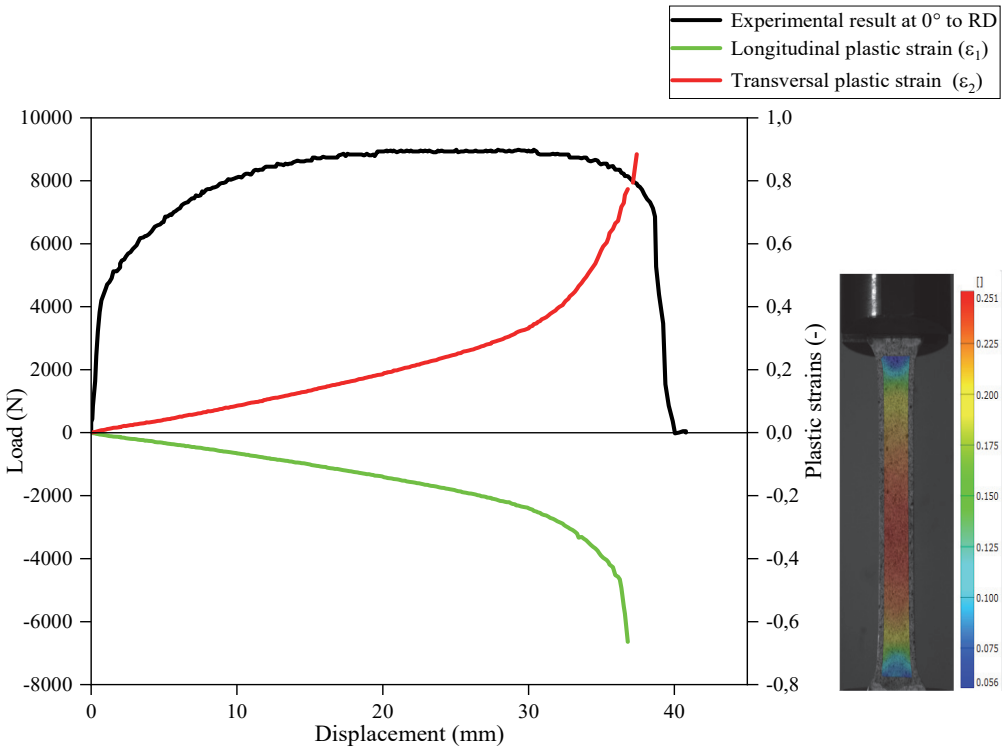

Figure 4: Data acquired from the tensile machine (Load vs. Displacement) and from the digital image correlation (Plastic strains vs. Displacement).

Their parameters were determined from Lankford's r-values using the following equations:

$$F=\frac{r_0}{r_{90}(1+r_0)},\quad G=\frac{1}{1+r_0},\qquad H=\frac{r_0}{1+r_0},\qquad N=\frac{(1+2r_{45})(r_0+r_{45})}{2r_{90}(1+r_0)} \tag{3}$$

An inverse numerical procedure was adopted to determine the parameters of isotropic rheological hardening laws for the DC06EK sheet metal using the numerical model of the tensile test under the same operating conditions. Two different hardening laws were selected:

$$Ludwick: \quad \sigma=\sigma_0+K\left(\varepsilon_p\right)^n \tag{4}$$

$$Voce: \quad \sigma=\sigma_s-\left(\sigma_s-\sigma_0\right)exp\left(-\alpha\left(\varepsilon_p\right)\right) \tag{5}$$

Here σ and ε_p represent the equivalent plastic stress and equivalent plastic strain, respectively, while σ_0, σ_s, α, K, and n denote the yield stress, the saturated yielding stress, the hardening parameter, the material consistency, and the hardening exponent, respectively. The inverse numerical procedure was executed using the software package Abaqus/Standard. Within this software, a UHARD subroutine was employed to implement the hardening laws. This numerical procedure, based on the FE model, was integrated with an optimization tool to minimize the disparity between numerical results and experimental data. The optimization tool utilized, known as "OPTPAR," was developed by Gavrus [28]. The optimal hardening law parameters were determined through the Gauss-Newton iterative algorithm, which aims to minimize the cost function [28–31]. This function is defined as:

$$Q = \frac{\sum_{i=1}^{Np}\left(\overline{F}_{exp}^{i} - \overline{F}_{num}^{i}\right)^2}{\sum_{i=1}^{Np}\left(\overline{F}_{exp}^{i}\right)^2} \tag{6}$$

with $\overline{F}_{exp}$: experimental data, $\overline{F}_{num}$: numerical results, and i = 1, 2, … to N_p: total number of experimental measures (or computed). The comparison between experimental and numerical load versus displacement is presented in Fig. 5. The identification by inverse procedure shows a good agreement of the identified hardening law parameters with experimental results. The resulting mechanical properties are also reported in Tab. 1.

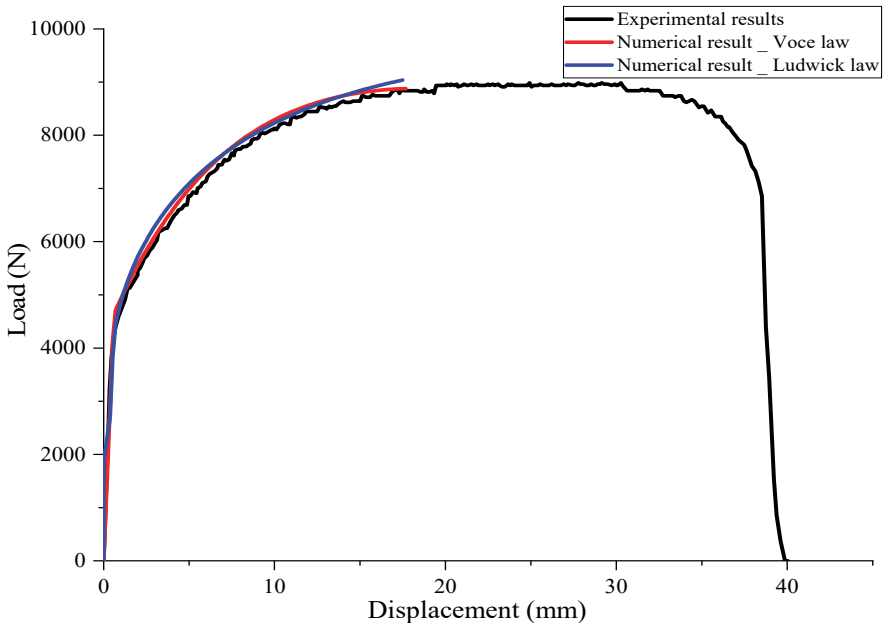

Figure 5: Comparison between experimental and numerical load vs. displacement after identification of hardening law parameters.

Rolling direction [°]	0° RD	90° RD	45° RD
Lankford's r-values [-]	2.826	2.689	1.959
Young's modulus E [GPa]		203	
Poisson's ratio ν [-]		0.3	
Yield stress $R_{p0.2}$ [MPa]	150	143	145
Ultimate tensile stress R_m [MPa]	281	290	295
Elongation A [%]	40	38	36
Material consistency K [-]		517.64	
Hardening exponent n [-]		0.423	
Saturated yielding stress σ_s [MPa]		340	
Hardening parameter α [-]		9	

Table 1: Mechanical properties of the DC06EK.

The formability of DC06EK sheet metal was predicted using the Keeler and Brazier model [32,33]. This model is used to represent the forming limit curve (FLC). The FLC indicates the boundary between deformation modes without defects and those with risks of necking, rupture, and wrinkling. This model is expressed as a function of the sheet metal thickness "t_0" and the work hardening coefficient "n" in order to determine the FLC for mild steels. The variable under consideration is

the position of the lowest point on the FLC, which is situated on the plane strain trajectory and denoted as "FLC_0". According to this model, the FLC is determined as follows:

$$FLC_0 = \ln\left(\frac{n}{0.116}\left(0.2325 + 0.1413.t_0\right) + 1\right) \tag{7}$$

$$\textit{Left side of the FLC}: \quad \varepsilon_1 = FLC_0 - \varepsilon_2 \tag{8}$$

$$\textit{Right side of the FLC}: \quad \varepsilon_1 = \left(FLC_0 + 1\right)\left(\varepsilon_2 + 1\right)^{0.5} - 1 \tag{9}$$

Friction

In the extra-deep drawing process of the wheelbarrow tray, a mineral oil-based lubricant named Torjan 460 – G006 is used at tool-blank contacts. The intention of using this lubricant is to facilitate the smooth flow of the blank between the blank holder and the die. To evaluate the coefficient of friction of the DC06EK steel under the same sliding contact conditions encountered in the wheelbarrow tray's extra-deep drawing process, a pin-on-disc test was conducted according to the ASTM G99 standard [34] (Fig. 6). In this setup, a disc-shaped sample (Fig. 6-a) was cut from the as-received DC06EK sheet metal and subjected to a rotary motion with various sliding velocities. The disc came into contact with a stationary ball measuring 6 mm in diameter (Fig. 6-b), which was subjected to an axial compressive load of 1N. The test was carried out under lubricated conditions at room temperature, using the same lubricant. The coefficient of friction was calculated as the ratio between the actual friction force and the normal force, which were measured during the tribological tests.

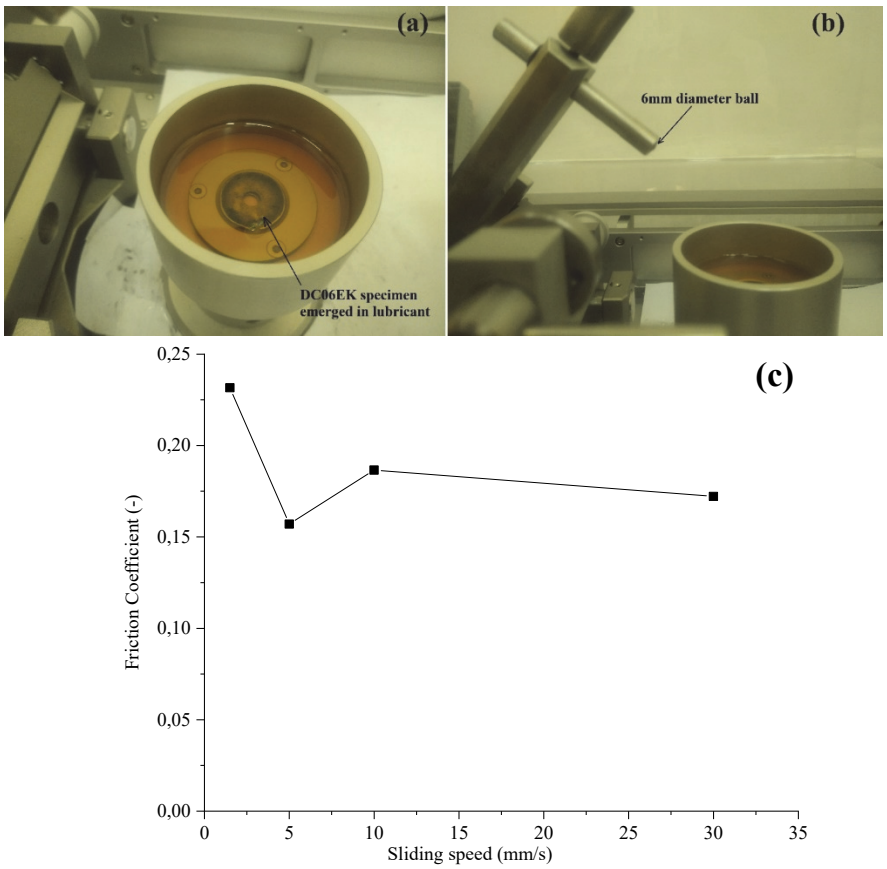

Figure 6: Ball-on-disc tribometer: (a) DC06EK disc sample immersed in lubricant, (b) Ball holder, (c) Coefficient of friction versus different sliding velocities.

Fig. 6-c illustrates the variation of the coefficient of friction with different sliding velocities. It is noted that the friction is slightly high for low sliding speeds, then decreases initially and remains relatively constant from a sliding velocity of 5 mm/s onwards. Based on these results, it is assumed that the coefficient of friction between the blank and the various tools is approximately 0.175 for different sliding velocities.

NUMERICAL MODELING

In this section, the objective is to perform numerical modeling with the same industrial parameters used in the EIMS company. The Abaqus/Explicit FE software was used, and the various stages of the numerical modeling process are outlined as follows:

Geometry and mesh

In the numerical modeling, the geometry of the punch is imported into ABAQUS/Explicit in the "IGES" format from the 3D laser scanning data, because the punch represents the most geometrically complex part. The other components are directly created within ABAQUS. The assembly of the various tools with the blank is represented in Fig. 7-a. The tools are considered rigid without deformation due to their high stiffness, while the blank is modeled as a deformable body. To mesh the blank, the S4R element type, a four-node quadrilateral shell element capable of deformation in a transverse shear plane, was employed [35,36]. For the tools, the R3D3 mesh type was chosen with refinement in the fillet regions (Fig. 7-b).

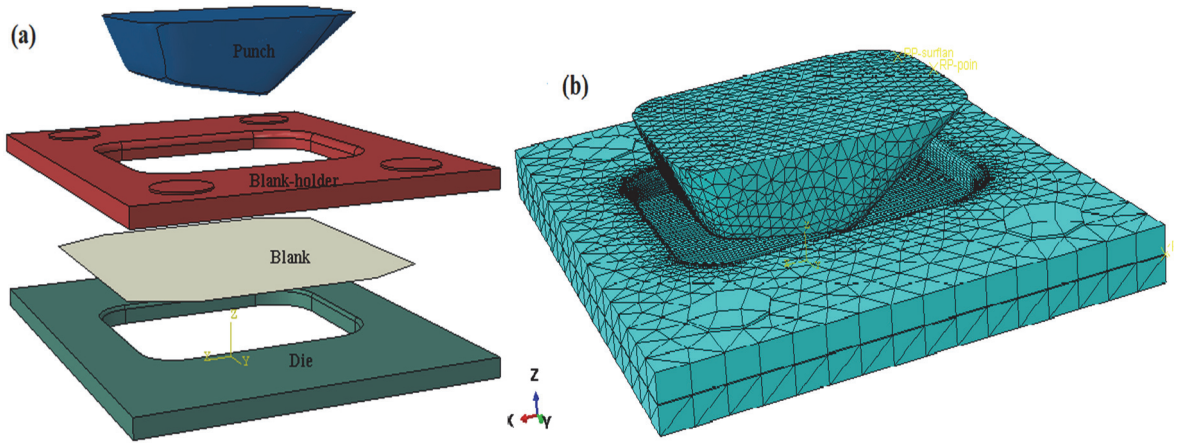

Figure 7: Finite-element model: (a) Tools and blank assembly, (b) Mesh of the different parts.

In finite element analysis, mesh density is an important parameter for achieving accurate results. On one hand, a smaller element size for discretizing the blank provides precision in the results. On the other hand, a finer mesh increases computation time. Then, a mesh sensitivity analysis was conducted for five different mesh sizes of the blank, as illustrated in Fig. 8-a and detailed in Tab. 2. This analysis focused just on the blank since it is considered deformable. The sizes of finite elements correspond to dividing the blank (1×1 m²) into 200×200, 125×125, 100×100, 67×67, 50×50, and 40×40 elements. Mechanical properties, contact conditions, and boundary conditions are provided in the subsections below.

Mesh	Name of different meshes	Number of Elements	Elements Size (mm)	Relative CPU Time (hr:min:sec)
Very fine	Mesh 1	35292	5 × 5	03:57:28
	Mesh 2	13716	8 × 8	00:57:41
Fine	Mesh 3	8840	10 × 10	00:30:39
Normal	Mesh 4	3920	15 × 15	00:10:16
Coarse	Mesh 5	2236	20 × 20	00:05:12
	Mesh 6	1428	25 × 25	00:03:04

Table 2: CPU time results for different mesh sizes.

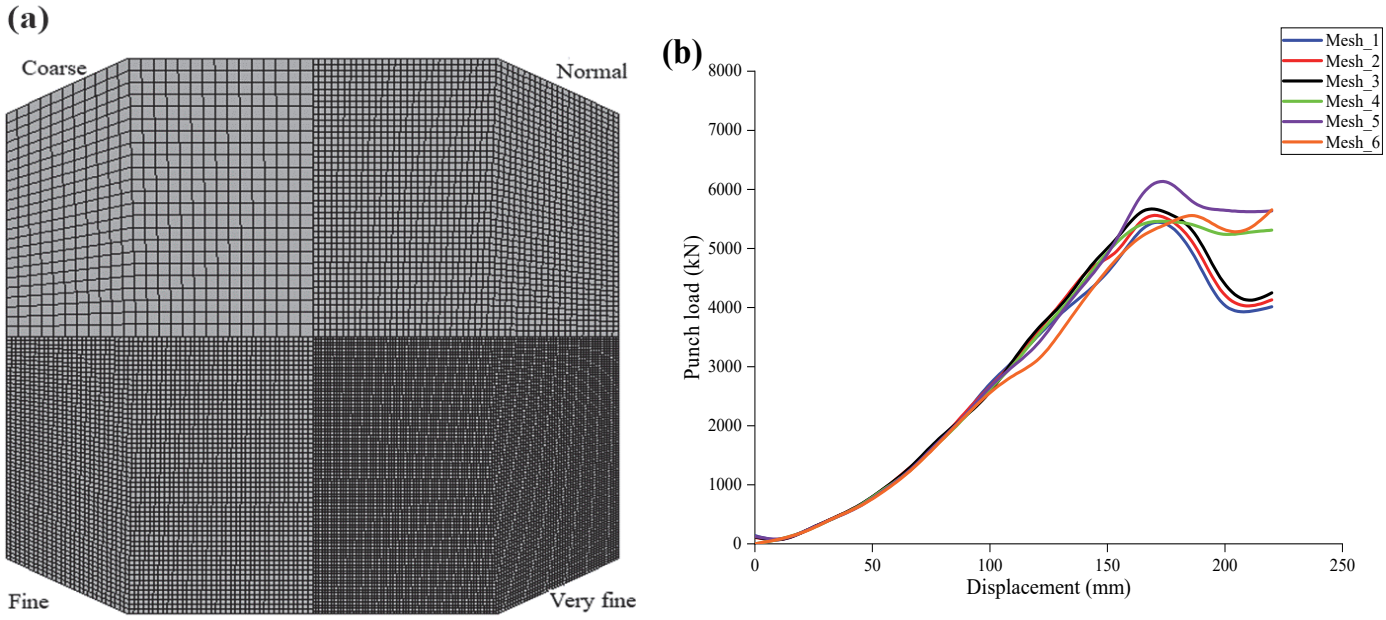

Figure 8. Mesh sensitivity analysis: (a) Illustration of different meshes and (b) Punch load vs. displacement results for various meshes.

The mesh sensitivity effect was evaluated based on the reaction of the punch load. Fig. 8-b depicts the punch load versus its displacement for the five different meshes. It is observed that the coarse and normal meshes predict the punch load less accurately, while the fine and very fine meshes yield similar results. From this mesh sensitivity analysis, the fine mesh is chosen for the numerical simulation due to its better-converged results and lower CPU time compared to the very fine mesh (Tab. 2). The number of elements and the mesh type for each part used in the numerical modeling are presented in Tab. 3.

Pieces	Element number	Meshing type
Punch	4886	Triangular « R3D3 »
Die	7846	Triangular « R3D3 »
Blank-holder	6922	Triangular « R3D3 »
Blank	8840	Quadrilateral « S4R »

Table 3: Mesh type and number of elements of the parts.

Material

The DC06EK steel sheet used in the numerical simulation was represented with anisotropic elastoplastic behavior. The elastic behavior was described using Hooke's model, incorporating a Young's modulus of E = 210000 MPa and a Poisson's ratio of ν = 0.3. Concerning the plastic behavior, the Hill48 anisotropic yield criterion associated with Voce's hardening law was used in the numerical modeling. The parameters of Hill48 were introduced directly in ABAQUS/Explicit. However, the implementation of Voce's hardening law (Eqn. 3) was achieved in ABAQUS/Explicit through a VUHARD subroutine. The parameters of the Hill48 criterion and the Voce's hardening law are described in the "Mechanical properties of the DC06EK" section.

Tools-blank contacts

At the start of the numerical simulation, the blank was positioned between the die and the blank holder. The punch, meanwhile, was adjusted in direct contact with the lower surface of the blank. To define these direct contact surfaces in the numerical model, a "Surface to surface" type of contact was employed, utilizing the "Slave-Master" concept. This specific type of contact describes the mechanical interaction between a deformable surface (the blank) and a rigid surface (the die, punch, and blank holder) in the numerical model. The "Surface to surface" contact was applied to the following interfaces: blank-die, blank-punch, and blank-blank holder (Fig. 9).

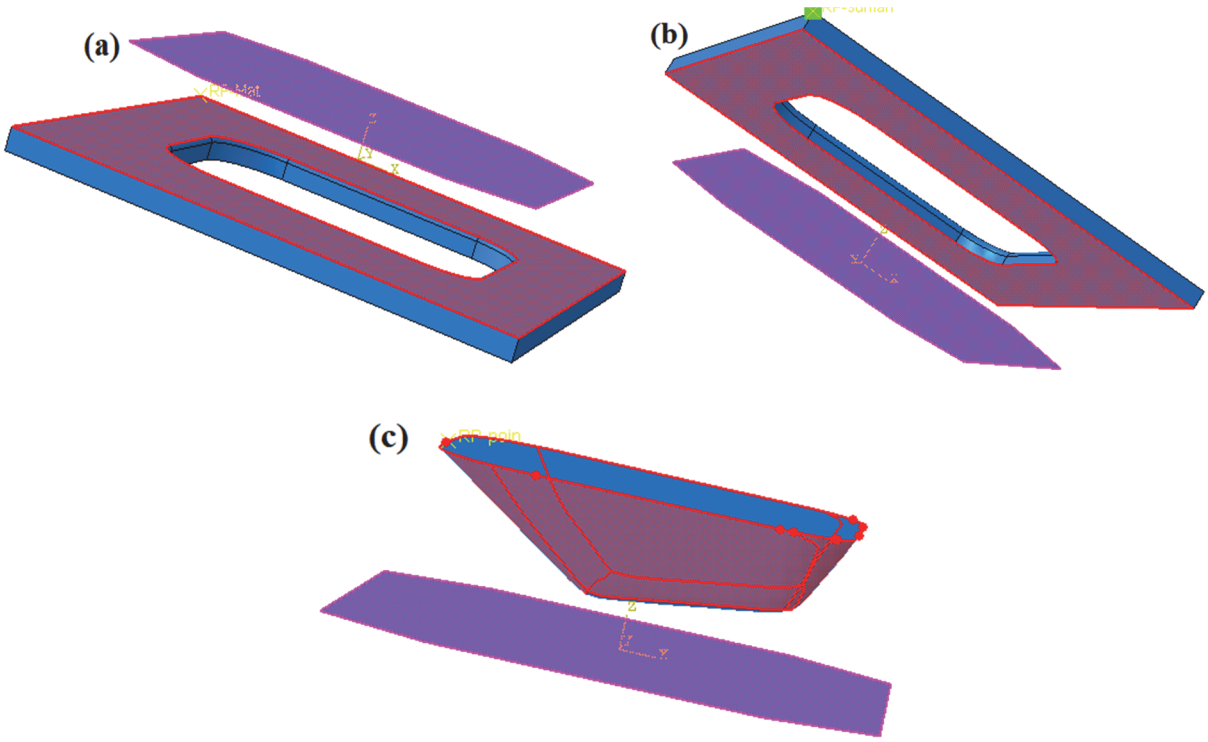

Figure 9: Tools-blank contacts: (a) Sheet metal-blank holder, (b) Punch-sheet metal, (c) Die-sheet metal.

In the extra-deep drawing operation, all of these contact surfaces were assumed to be lubricated. Coulomb's law was employed to describe the friction between the blank and the various tools. A uniform coefficient of friction of "0.175" was considered for all contact interfaces. This coefficient was measured from the pin-on-disc test results, as explained in the "friction" section.

Boundary conditions

Appropriate boundary conditions were applied in the numerical model, as depicted in Fig. 10. These boundary conditions define the movements and degrees of freedom for the different tools in the numerical simulation exactly like the real operation in the EIMS company.

The following boundary conditions were applied:

1. A displacement of 220mm was applied to the punch along the z-direction. This movement was carried out at a constant speed during the forming process.
2. Blank-Holder Pressure (BHP):
    a. The BHP consists of four independently controlled actuators (Fig. 10).
    b. A pressure of 50 MPa was applied to each actuator situated on the upper surface of the blank holder. This pressure was what the machine's operator put on the press to obtain a defect-free manufactured wheelbarrow tray.
    c. Other pressures are applied to investigate and analyze the appearance of rupture and wrinkling defects. The goal is to fix the lower and higher pressures applied to the BHP to obtain a defect-free product.
    d. The different pressures applied are maintained at a constant level throughout the entire deep drawing operation.
3. The die was considered to be fully embedded, meaning it was held in a fixed position during the simulation.

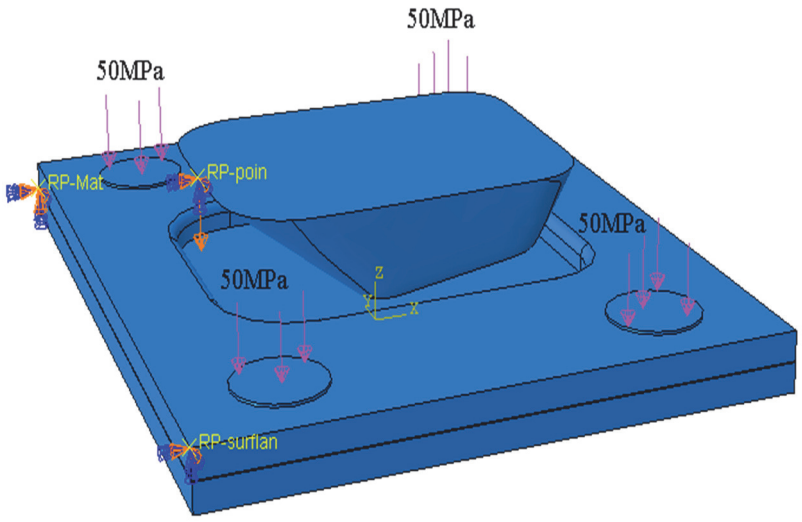

Figure 10: Boundary conditions and loading applied to various components in the extra-deep drawing tools.

RESULTS AND DISCUSSION

Experimental and numerical comparison

A comparison was conducted between the numerical results and the ultrasonic thickness measurements to validate the numerical approach. The variation in thickness after the sheet metal forming process is one of the major quality characteristics, and it is directly related to stress and strain distribution during the deep drawing. Thus, measuring the variation in thickness reveals the critical areas at the deep-drawn wheelbarrow tray and the location of the neck prior to rupture. In order to analyze thickness reduction in the wheelbarrow tray model, thickness changes were carefully evaluated along different paths: longitudinal (section A-A), transversal (section B-B), and diagonal (section C-C), as shown in Fig. 11. The comparison between the manually measured thickness changes and those determined by the numerical simulation reveals a very good agreement, confirming that the numerical simulation of the wheelbarrow tray corresponds well to the real case manufactured at the EIMS company. However, certain small differences, particularly following Section B-B, can be attributed to several factors:

- The used sheet metal doesn't have a uniform thickness of 1.6mm throughout.
- The introduction of elastoplastic behavior in the Abaqus code requires precise characterization of the sheet metal. For example, it is important to see other anisotropic yield criteria;
- The friction and contact conditions between the sheet metal and the tools play a significant role. Determining the coefficient of friction must account for the materials of the different tools, their surface finishing, and mixed lubrication in the numerical model.

Note that the reduction in thickness is greater in the areas that coincide with the corners of the wheelbarrow tray. These significant deformations are explained by the contact of the blank with the punch corner radii. In these areas, the thickness is reduced from 1.6mm to 1mm (refer to Fig. 11 - section C-C). Various studies also show that the minimum thicknesses were detected at the punch corner radii in both the simulation and experiment [3,37]. The thicknesses observed are always greater than 1mm, which means that the deformation in the thickness does not exceed 35%. These results are confirmed by the thickness reduction cartography in the wheelbarrow tray in Fig. 11-d after forming operation according to a final punch travel of 220mm, where the thickness is reduced from 1,6mm to 1.035 mm.

Formability

Using Eqns. (4, 5, and 6), two theoretical FLCs were obtained for DC06EK sheet metal with thicknesses of 1.6mm and 1mm. The latter was then compared with the experimental FLC obtained from punch stretches tests following the Nakazima method [38], as illustrated in Fig. 12. The comparison demonstrated a good agreement between the experimental and theoretical FLCs for the 1mm sheet thickness. Moreover, the FLC increased for the 1.6mm thickness used in this research work.

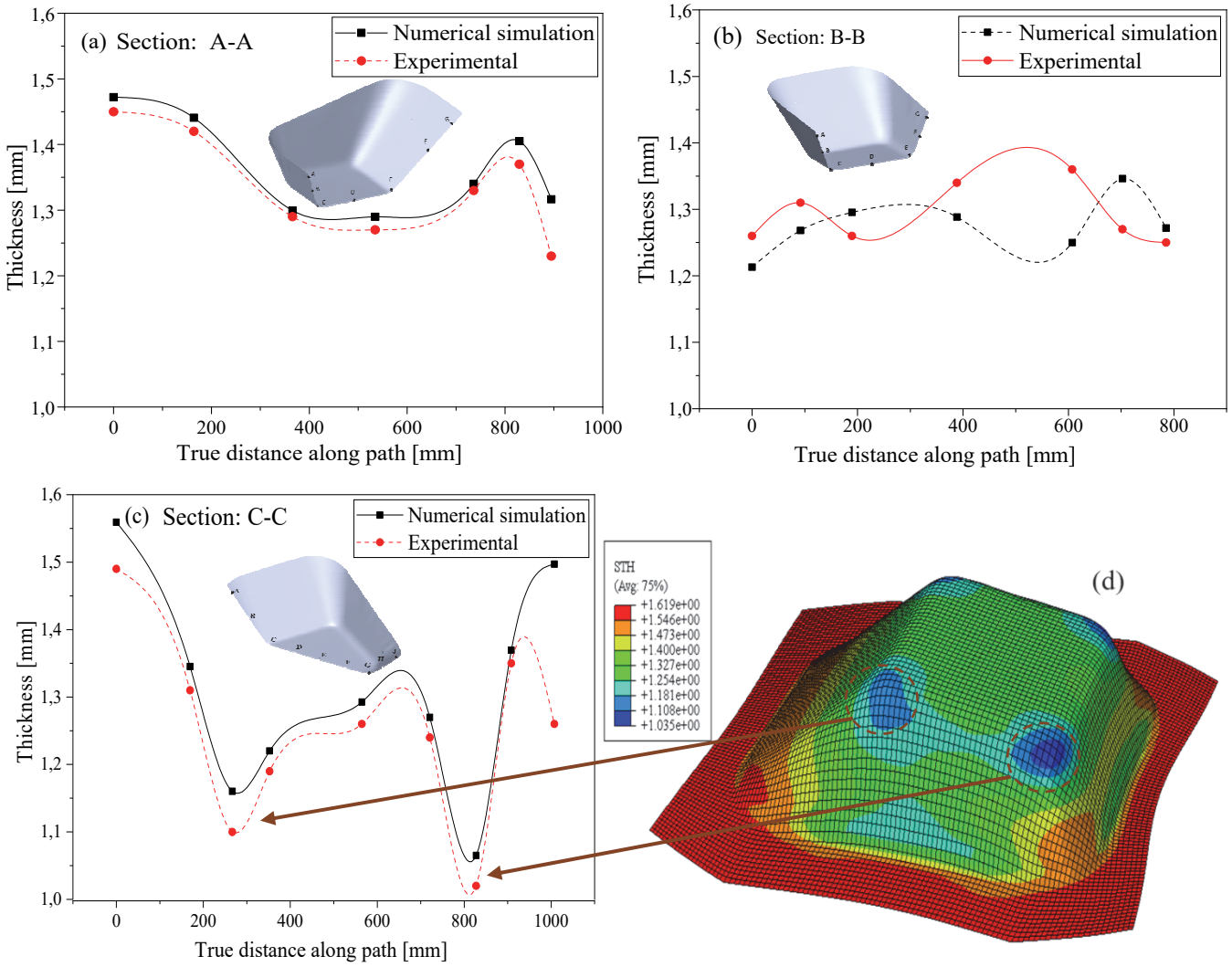

Figure 11: Experimental and numerical analysis of thickness reduction in the wheelbarrow tray.

To ensure that the material in the deep-drawn wheelbarrow tray doesn't experience necking or rupture, it's important for the limit strains to remain consistently below the FLC. Typically, a safety margin of around 10% is applied by setting the FLC slightly lower [39]. This safety margin helps assess the risk of necking by examining how closely the limit strains approach the FLC. Evaluating the numerical simulation of the wheelbarrow tray's extra-deep drawing process using the FLC, the consistent application of a BHP of 50 MPa throughout the entire deep-drawing process yielded limit strains positioned within the safe area of the FLC (refer to Fig. 12-a). No instances of necking or rupture were identified in this context. These outcomes also underscored that the material exhibits very good formability.

As we have argued, rejection of the manufactured product can occur due to issues beyond just necking or rupture, like wrinkling. This latter tends to occur when there's a thin sheet of material subjected to compressive stress. The risk of wrinkling is particularly high when the material undergoes strain paths ranging from uniaxial compression to pure shear. At the same time, there's also a noticeable tendency for wrinkling in situations where the strain paths go from pure shear to uniaxial tension. In the case of a BHP of 50 MPa, all limit strains are out of the wrinkling zone (Fig. 12-a). When the BHP is increased or decreased in the numerical model, rupture or wrinkling defects are obtained (Figs. 12-b and 12-c). It was found that the appearance of rupture took place at a BHP of 70 MPa. However, the wrinkling appeared for BHP below 20 MPa. Therefore, the pressure that must be applied to the BHP must be between these last two values (20 and 70 MPa) to obtain a defect-free wheelbarrow tray.

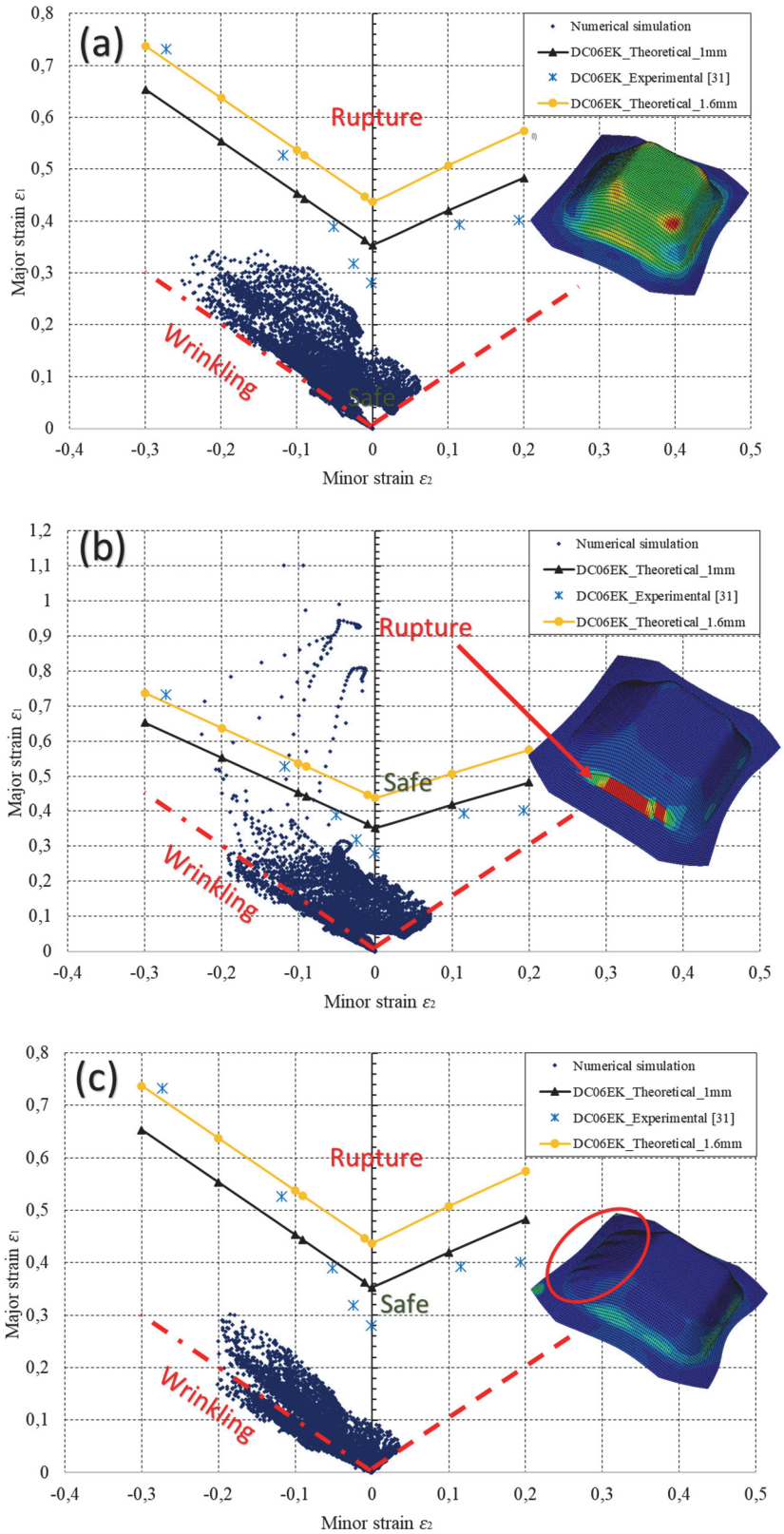

Figure 12: Comparison of experimental FLC of the DC06EK with the Keeler-Brazier equation and numerical simulation-derived limit strains for the wheelbarrow tray for three different BHP: (a) 50 MPa, (b) 70 MPa, (c) 20 MPa.

Displacement fields

The displacement field from numerical simulation can provide a clear visualization of the wrinkling defect. Fig. 13 represents the displacement cartographies in the z-direction (deep-drawing direction) for the three different pressures (20, 50, and 70 MPa) applied to the BHP. It can be noted that the displacement imposed on the punch of 220mm is reached during deep drawing in all three cases. The displacement cartographies confirm that there is no wrinkling in the case of a BHP of 50 MPa, which corresponds to the real case of the finished product (Fig. 13-a). The same remark was made for the case of BHP of 70 MPa (Fig. 13-b), since the limit strains exceeded the formability limits and there was a rupture defect. However, the wrinkling is clearly visible in the case of a BHP of 20 MPa (Fig. 13-c). These results confirm the above results ("Formability" section). We can say that the pressure applied to the BHP is a very important operating parameter to obtain a defect-free product since it makes it possible to control the flow of the blank between the blank holder and the die during the extra-deep drawing operation.

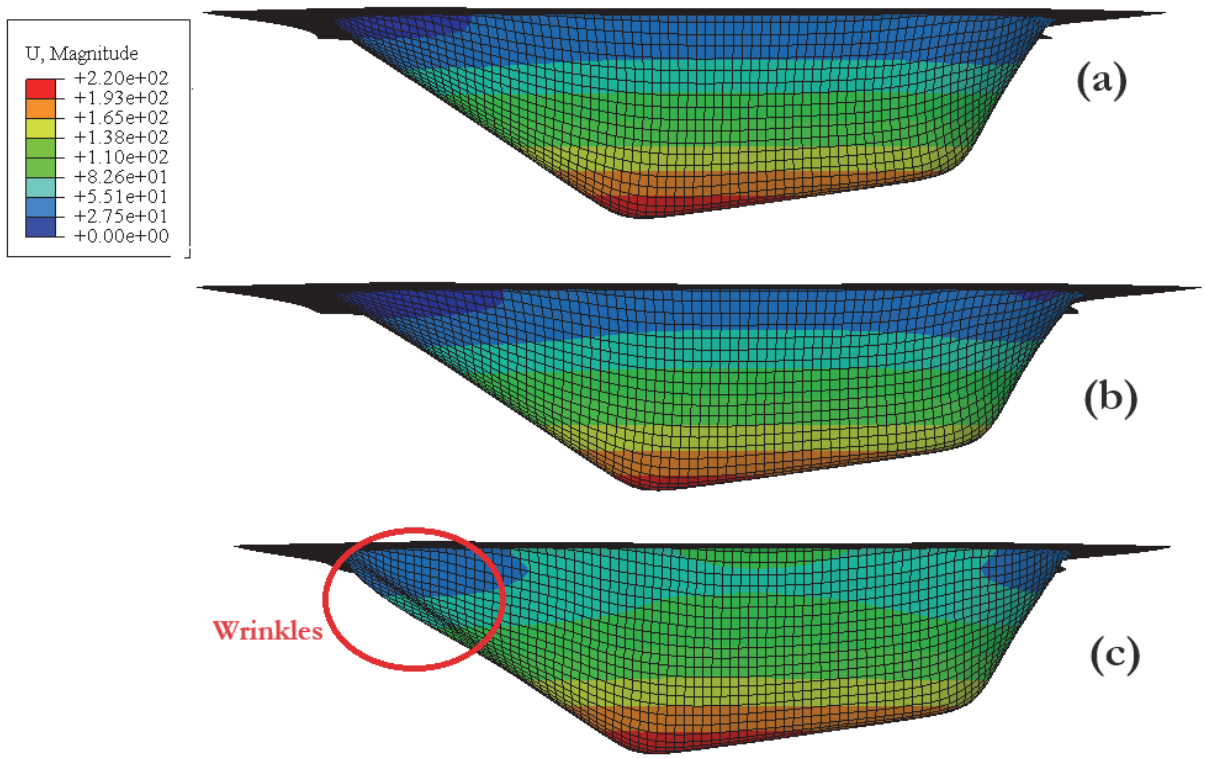

Figure 13: Displacement cartographies in the deep drawing direction for the three different BHP: (a) 50 MPa, (b) 70 MPa, (c) 20 MPa.

Punch load

The punch load versus displacement behavior is a crucial characteristic for process optimization and quality control. It is influenced by various factors, including friction at the blank-tool contacts, mechanical properties of the sheet material, BHP, and punch speed [40–42]. Fig. 14 displays punch load versus displacement traces obtained from numerical simulations of the wheelbarrow tray's extra-deep drawing process. The drawing punch load increases, peaking at approximately 5630 kN for a BHP of 50 MPa and 7283 kN for a BHP of 70 MPa, with a punch displacement of about 150 mm. At this stage, the punch load must overcome several factors, including the sheet metal's strength, frictional resistance at the blank-tool contacts, especially at the shoulder radii of the cavity die and the punch corner radii, as well as the pressure applied to the blank holder. These peak drawing loads coincide with the moment when the blank is fully formed within the die shoulder radii and punch corner radii, resulting in excellent surface quality without wrinkling in both cases (50 MPa and 70 MPa). Subsequently, the required drawing load decreases or becomes constant since the frictional resistance decreases. However, this is not the case with a BHP of 20 MPa, as wrinkles form in the wheelbarrow tray and the load continues to increase without a clear peak.

The area under the punch load versus displacement curve represents the work done on the material during the forming process. This work corresponds to the total energy consumed during the process. Analyzing the punch load versus displacement curve can assist engineers and manufacturers in optimizing the forming process to reduce energy consumption.

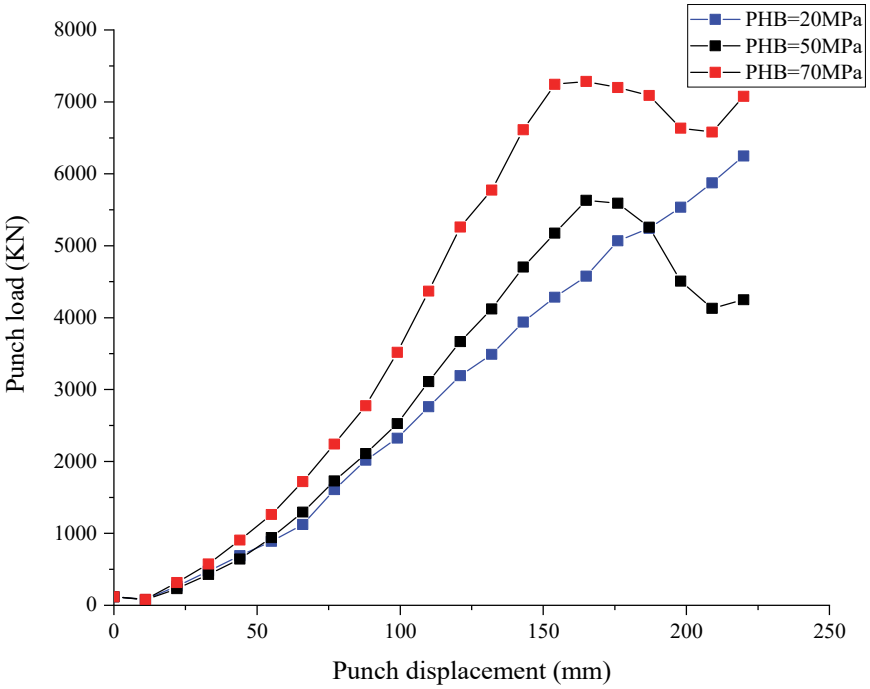

Figure 14: Punch load vs. displacement for different BHP.

CONCLUSIONS AND PROSPECTS

In this study, a successful investigation of a wheelbarrow tray's extra-deep drawing process was conducted using numerical simulations based on Abaqus/Explicit FE software. The numerical results were validated through a comprehensive comparison with experimental data, including ultrasonic thickness measurements. Successful numerical simulation of a deep drawing process requires:

- Geometric modeling with dimensions of the sheet metal and different tools as used in reality, and it will be useful to use 3D scanners in the case of complex geometries.
- Tool actions modeling as used in the deep drawing machine.
- The accurate determination of the rheological, tribological behavior, and the FLC or a damage law for the used sheet metal based on appropriate mechanical tests.

The numerical and experimental results showed that the thickness reduction was found to be more significant in the corners of the wheelbarrow tray due to the contact of the blank with the punch corner radii. Numerical simulation findings indicated that the extra-deep drawing process for the chosen DC06EK sheet exhibited excellent formability, with no wrinkling, necking, or rupture identified for a pressure of 50 MPa applied to each actuator situated on the upper surface of the blank holder. This pressure was applied by the machine's operator to ensure a defect-free manufactured wheelbarrow tray. In this study, it was found that pressures lower than 20 MPa can cause wrinkling and pressures higher than 70 MPa can cause necking or rupture, and between the two cases, a safe product is obtained.

From the outcomes, it can be concluded that the pressure applied directly to the blank holder fixes and controls the flow of the blank between the blank holder and the die during the deep-drawing operation, which is essential for obtaining a defect-free product. Since the BHP is made up of four independently controlled actuators, different pressures within the determined limits (from 20 to 70 MPa) can be numerically investigated on the four actuators to obtain a high-quality product with low thickness thinning. This can also be used to optimize the punch load versus displacement curve to reduce energy consumption.

This numerical model also makes it possible to investigate other materials such as DC05EK and DC04EK, which have less formability, are more adaptive to enameling, and are less expensive than DC06EK. However, it is necessary to repeat the rheological and tribological characterizations, as was done in this study, to introduce reliable data on these sheet materials into a numerical calculation code.
This study provides valuable insights into the extra-deep drawing process. As a future prospect, further investigations could focus on extending the study to include other sheet metal materials and complex geometries can provide a broader understanding of the extra-deep drawing process and its applicability in various industrial sectors. Collaborating with industry partners and conducting real-world trials could facilitate the implementation of the research findings in practical manufacturing processes, contributing to increased productivity and cost savings.

ACKNOWLEDGEMENTS

This work is supported by EIMS-Miliana company, the Algerian Ministry of Higher Education and Scientific Research, and the Directorate General for Scientific Research.

REFERENCES

[1] Padmanabhan, R., Oliveira, M.C., Alves, J.L., Menezes, L.F. (2008). Numerical simulation and analysis on the deep drawing of LPG bottles, J. Mater. Process. Technol., 200(1), pp. 416–423, DOI: 10.1016/j.jmatprotec.2007.08.047.
[2] Ghennai, W., Boussaid, O., Bendjama, H., Haddag, B., Nouari, M. (2019). Experimental and numerical study of DC04 sheet metal behaviour—plastic anisotropy identification and application to deep drawing, Int. J. Adv. Manuf. Technol., 100(1), pp. 361–371, DOI: 10.1007/s00170-018-2700-8.
[3] Tomáš, M., Evin, E., Kepič, J., Hudák, J. (2019). Physical Modelling and Numerical Simulation of the Deep Drawing Process of a Box-Shaped Product Focused on Material Limits Determination, Metals (Basel)., 9(10), pp. 1–16, DOI: 10.3390/met9101058.
[4] EIMS. EIMS.(2023). Entreprise industrielle de materiel sanitaire (EIMS-Miliana), Algeria. Available at: https://www.eimsanitaire.dz/. [accessed October 1, 2023].
[5] Tiwari, P.R., Rathore, A., Bodkhe, M.G. (2022). Factors affecting the deep drawing process – A review, Mater. Today Proc., 56, pp. 2902–2908, DOI: 10.1016/j.matpr.2021.10.189.
[6] Atul S, T., Babu, M.C.L. (2019). A review on effect of thinning, wrinkling and spring-back on deep drawing process, Proc. Inst. Mech. Eng. Part B J. Eng. Manuf., 233(4), pp. 1011–1036, DOI: 10.1177/0954405417752509.
[7] Candra, S., Batan, I.M.L., Berata, W., Pramono, A.S. (2015). Analytical Study and FEM Simulation of the Maximum Varying Blank Holder Force to Prevent Cracking on Cylindrical Cup Deep Drawing, Procedia CIRP, 26, pp. 548–553, DOI: 10.1016/j.procir.2014.08.018.
[8] Sorrentino, L., Parodo, G., Giuliano, G. (2022). Lightweight structures: An innovative method to uniform the thickness of metal sheets by patchwork blanks, Int. J. Light. Mater. Manuf., 5(1), pp. 20–28, DOI: 10.1016/J.IJLMM.2021.08.003.
[9] Parodo, G., Giuliano, G., Sorrentino, L. (2020). Uniformity of thickness of metal sheets by patchwork blanks: potential of adhesive bonding, Frat. Ed Integrità Strutt., 14(53 SE-Advanced Manufacturing and Processing), pp. 166–176, DOI: 10.3221/IGF-ESIS.53.14.
[10] Neto, D.M., Oliveira, M.C., Santos, A.D., Alves, J.L., Menezes, L.F. (2017). Influence of boundary conditions on the prediction of springback and wrinkling in sheet metal forming, Int. J. Mech. Sci., 122, pp. 244–254, DOI: 10.1016/j.ijmecsci.2017.01.037.
[11] Bahanan, W., Fatimah, S., Go, J.H., Oh, J.M., Kim, M.J., Kim, M.J., Kang, J.-H., Kim, D.-J., Widiantara, I.P., Ko, Y.G. (2023). A Finite Element Analysis of Cold Deep Drawing of Al Alloy Considering Friction Condition and Corner Design of Plunger, Lubricants, DOI: 10.3390/lubricants11090388.
[12] Kim, H., Sung, J.H., Sivakumar, R., Altan, T. (2007). Evaluation of stamping lubricants using the deep drawing test, Int. J. Mach. Tools Manuf., 47(14), pp. 2120–2132, DOI: 10.1016/j.ijmachtools.2007.04.014.
[13] Pan, D., Zhang, G., Wu, H., Jia, F., Li, L., Zhang, T., Yang, M., Jiang, Z. (2023). Tribological behaviour of ultra-thin stainless steel in micro deep drawing with graphene nanosheets, Wear, 524–525, pp. 204878, DOI: 10.1016/j.wear.2023.204878.

[14] Miloud, M.H., Zidane, I., Mendas, M. (2019). Coupled identification of the hardening behavior laws and Gurson–Tvergaard–Needleman damage parameters - validation on tear test of 12NiCr6 CT specimen, Frat. Ed Integrita Strutt., 13(49), DOI: 10.3221/IGF-ESIS.49.57.
[15] Reddy, R.V., Reddy, T.A.J., Reddy, G.C.M. (2012). Optimization of Blank Holder Force to Control Wrinkling and Fracture of Cylindrical Cups in Deep Drawing, Int. J. Eng. Trends Technol., 3(5), pp. 669–676.
[16] Heingärtner, J., Bonfanti, D., Harsch, D., Dietrich, F., Hora, P. (2018). Implementation of a tribology-based process control system for deep drawing processes, IOP Conf. Ser. Mater. Sci. Eng., 418, pp. 12112, DOI: 10.1088/1757-899x/418/1/012112.
[17] Padmanabhan, R., Oliveira, M.C., Alves, J.L., Menezes, L.F. (2007). Influence of process parameters on the deep drawing of stainless steel, Finite Elem. Anal. Des., 43(14), pp. 1062–1067, DOI: 10.1016/j.finel.2007.06.011.
[18] Khelifa, M., Oudjene, M. (2008). Numerical damage prediction in deep-drawing of sheet metals, 0, pp. 71–76, DOI: 10.1016/j.jmatprotec.2007.08.041.
[19] Bunyan, T., Yiemchaiyaphum, S., Panich, S. (2020). Wrinkling prediction of rectangular cup deep drawing process for aluminum alloy sheets by using the modified yoshida buckling test, Key Eng. Mater., 856 KEM, pp. 143–151, DOI: 10.4028/www.scientific.net/KEM.856.143.
[20] Hamza, F., Boussaid, O., Tadjine, K. (2017). Study by numerical simulation of the deep drawing parameters-material during the wheelbarrow forming, Mater. Sci. Forum, 895 MSF, pp. 94–98, DOI: 10.4028/www.scientific.net/MSF.895.94.
[21] Habibi, N., Sundararaghavan, V., Prahl, U., Ramazani, A. (2018). Experimental and Numerical Investigations into the failure mechanisms of TRIP700 steel sheets, Metals (Basel)., 8(12), pp. 1–17, DOI: 10.3390/met8121073.
[22] Luo, M., Li, Y., Gerlach, J., Wierzbicki, T. (2010). Prediction of Shear-induced Crack Initiation in AHSS Deep Drawing Operation with a Phenomenological Fracture Model, AIP Conf. Proc., 1252, pp. 464–472, DOI: 10.1063/1.3457591.
[23] Abbadeni, M., Zidane, I., Zahloul, H., Madaoui, Z. (2019). Comparative study of conventional and hydromechanical deep drawing processes based on finite element analysis, Frat. Ed Integrita Strutt., 13(49), DOI: 10.3221/IGF-ESIS.49.28.
[24] Zidane, I., Guines, D., Léotoing, L., Ragneau, E. (2010). Development of an in-plane biaxial test for forming limit curve (FLC) characterization of metallic sheets, Meas. Sci. Technol., 21(5), pp. 055701, DOI: 10.1088/0957-0233/21/5/055701.
[25] American Society for Testing and Materials. (2022). ASTM E8/E8M – 22: Standard Test Methods for Tension Testing of Metallic Materials. 3.01, ASTM standards.
[26] International Standards Organization. (2020). ISO 10113: Metallic materials — Sheet and strip — Determination of plastic strain ratio, ISO.
[27] Hill, R. (1993). A user-friendly theory of orthotropic plasticity in sheet metals, Int. J. Mech. Sci., 35(1), pp. 19–25, DOI: 10.1016/0020-7403(93)90061-X.
[28] Gavrus, A. (1996).Identification automatique des paramètres rhéologiques par analyse inverse. École Nationale Supérieure des Mines de Paris.
[29] Zidane, I. (2009).Développement d'un banc d'essai de traction biaxale pour la caracterisation de la formabilité et du comportement élastoplastique de tôles métalliques. Rennes, INSA.
[30] Hadj Miloud, M., Zidane, I., Mendas, M. (2019). Coupled identification of the hardening behavior laws and Gurson–Tvergaard–Needleman damage parameters - Validation on tear test of 12NiCr6 CT specimen, Frat. Ed Integrità Strutt., 13(49 SE-Articles), pp. 630–642, DOI: 10.3221/IGF-ESIS.49.57.
[31] Zidane, I., Guines, D., Leotoing, L., Ragneau, E. (2010). Development of an in-plane biaxial test for forming limit curve (FLC) characterization of metallic sheets, Meas. Sci. Technol., 21(5), pp. 55701.
[32] Keeler, S.P. (1977). Relationship between laboratory material characterization and press-shop formability, ,.
[33] Paul, S.K. (2021). Controlling factors of forming limit curve: A review, Adv. Ind. Manuf. Eng., 2, pp. 100033, DOI: 10.1016/j.aime.2021.100033.
[34] American Society for Testing and Materials. (2023). ASTM G99-17 - Standard Test Method for Wear Testing with a Pin-on-Disk Apparatus, ASTM standards.
[35] Önder, E., Tekkaya, A.E. (2008). Numerical simulation of various cross sectional workpieces using conventional deep drawing and hydroforming technologies, Int. J. Mach. Tools Manuf., 48(5), pp. 532–542.
[36] Kim, Y.S., Jain, M.K., Metzger, D.R. (2012). Determination of pressure-dependent friction coefficient from draw-bend test and its application to cup drawing, Int. J. Mach. Tools Manuf., 56, pp. 69–78, DOI: 10.1016/j.ijmachtools.2011.12.011.

[37] Şener, B., Kurtaran, H. (2016). Modeling the deep drawing of an AISI 304 stainless-steel rectangular cup using the finite-element method and an experimental validation, Mater. Tehnol., 50, pp. 961–965, DOI: 10.17222/MIT.2015.278.
[38] Liu, Z., Li, W., Shao, X., Kang, Y., Li, Y. (2019). An Ultra-low-Carbon Steel with Outstanding Fish-Scaling Resistance and Cold Formability for Enameling Applications, Metall. Mater. Trans. A, 50(4), pp. 1805–1815, DOI: 10.1007/s11661-018-05101-z.
[39] Holmberg, S., Enquist, B., Thilderkvist, P. (2004). Evaluation of sheet metal formability by tensile tests, J. Mater. Process. Technol., 145(1), pp. 72–83, DOI: 10.1016/j.jmatprotec.2003.07.004.
[40] Olguner, S., Bozdana, A.T. (2016). The effect of friction coefficient on punch load and thickness reduction in deep drawing process, Int. J. Mater., 3, pp. 64.
[41] Sugiyanto, D., Asbanu, H., Siahaan, F.S. (2020). The effect of blank holder on the deep drawing process on plates using software based with a Finite Element Method (FEM), J. Phys. Conf. Ser., 1469(1), pp. 12038, DOI: 10.1088/1742-6596/1469/1/012038.
[42] Coër, J., Laurent, H., Oliveira, M.C., Manach, P.-Y., Menezes, L.F. (2018). Detailed experimental and numerical analysis of a cylindrical cup deep drawing: Pros and cons of using solid-shell elements, Int. J. Mater. Form., 11(3), pp. 357–373, DOI: 10.1007/s12289-017-1357-4.